

Czech Technical University in Prague
Faculty of Civil Engineering
Department of Mechanics



Optimising truss-based metamaterials for unimodal and pentamodal behaviour

Nataša Jošková

Supervisors:

Ing. Martin Doškář, Ph.D.

Ing. Marek Tyburec, Ph.D.

Soutěž o cenu akademika Bažanta

Prague, April 2025

Acknowledgements

I would like to thank my supervisors, Martin Doškář and Marek Tyburec, for their unwavering support and guidance. I am also grateful to Jan Zeman for his insightful comments and valuable feedback. Additionally, I acknowledge support from the Czech Science Foundation, Project No. GA22-15524S.

Abstract

Our study focuses on optimisation of the internal structure of unimodal and pentamodal metamaterials, modelled as three-dimensional linear elastic lattice structures. For optimisation, we represent the metamaterials with discrete truss models of their respective Periodic Unit Cells (PUCs), whose effective response is determined by the first-order numerical homogenisation. The optimisation is formulated as an inverse homogenisation problem with objective functions comprising a ratio of selected eigenvalues of the effective stiffness matrix, which allows us to dispense with the traditional volume constraint and solve the optimisation problem with a simple gradient method combined with the line search method. We demonstrate the efficacy of the formulation with a design of a unimodal material compliant in a chosen shear deformation mode and we also show that our formulation recovers the traditional pentamodal metafluid. The response of optimised metamaterials is then evaluated using a geometrically nonlinear model, confirming that they preserve their multimodal behaviour even under large deformations.

Keywords

optimisation, unimodal metamaterial, pentamodal metamaterial, first-order homogenisation, Periodic Unit Cell, linear elastic model, geometrically nonlinear model

Contents

1	Introduction	1
2	Methodology	3
2.1	Numerical model	3
2.2	First-order homogenisation	4
2.3	Topology optimisation	5
3	Optimised metamaterials	8
3.1	Unimodal metamaterial	8
3.2	Pentamodal metamaterial	10
4	Geometrically nonlinear analysis	12
4.1	Numerical model	12
4.1.1	Residual vector	13
4.1.2	Stiffness matrix	14
4.2	Numerical strategy	16
4.3	Results	17
5	Summary	19

1 Introduction

Metamaterials have physical properties that surpass those commonly found in nature. Moreover, these unique properties arise primarily from the microstructure of metamaterials rather than the chemical or physical characteristics of their bulk constituents [1]. In our study, we focus on three-dimensional unimodal and pentamodal mechanical metamaterials [2]. The modality of these materials is derived from the number of free modes of deformation [3], i.e., homogeneous deformations that do not result in an increase in the stored strain energy. In particular, a unimodal metamaterial is pliable in one specific direction but very stiff in all other modes of deformation. On the other hand, pentamodal metamaterials behave like a fluid (sometimes pentamodal metamaterials are called metafluids), i.e., while they are almost incompressible, they can be easily deformed in a deviatoric way.

Because of their unique properties, these metamaterials can be applied in various advanced fields. One of the most extensively researched applications is their ability to create acoustic band gaps—specific frequency ranges in which sound waves are unable to propagate through the material due to disrupted transmission [4, 5]. This behaviour makes them highly effective for applications in noise control, vibration isolation, and acoustic filtering, even underwater [6]. Another potential application is for cloaking devices that transform waves to make objects invisible or undetectable by bending light or sound, effectively preventing detection or visual observation [7]. The ability to control the propagation of elastic waves also makes them highly effective for seismic isolation [8, 9].

Multimodal metamaterials have garnered significant research interest, with pentamodal metamaterials being a primary focus. However, much of the research involves modifying the original pentamodal structure introduced by Milton and Cherkaev [3] to enhance its overall performance. This includes investigating different shapes [10] and sizes [11] of cross-sectional areas, adding spherical masses to the nodes [12] and incorporating stiffening plates between the metamaterial layers [13], even with different microstructures [14]. In addition, researchers managed both to introduce anisotropy by shifting the central part of the microstructure [15, 16], and, conversely, employ symmetrical designs [17].

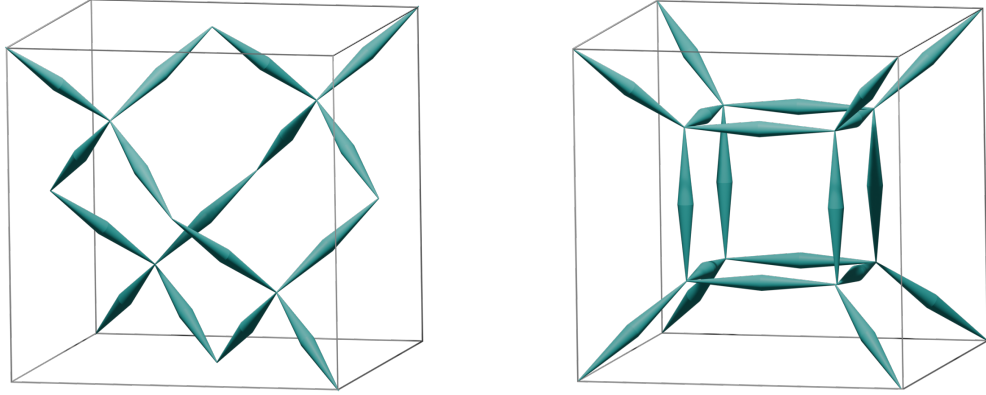


Figure 1.1: Examples of existing pentamodal materials: (left) a microstructure proposed by Milton and Cherkaev [3], and (right) an alternative design by Guo and coworkers [14].

In contrast, optimising metamaterial topology through inverse homogenisation, pioneered by the seminal work of Sigmund [18], often revolves around enhancing the bulk or shear modulus [19], tailoring Poisson’s ratio [20], and designing materials that are both lightweight and stiff [21] or that follow a predefined macroscopic response in the case of nonlinear models [22]. Relatively few studies have focused on optimising multimodal metamaterial microstructures. In addition to inverse homogenisation, genetic algorithms have been used to optimise the ratio of eigenfrequencies [23] and components of the homogenised stiffness matrix [24], or to maximise bandwidth [25] to improve the acoustic band gap.

In this work, we use inverse homogenisation with the objective function based on a ratio of effective stiffness’s eigenvalues (or its analogues), distinct from previously discussed approaches. Our approach allows for the optimisation of specific deformation modes and enables the analytical expression of the objective function’s gradient. In addition, it naturally avoids the need for the volume constraint.

To keep this contribution self-contained, the Methodology section next briefly introduces the linear model with discrete truss elements (Section 2.1) and covers the essentials of the first-order homogenisation (Section 2.2) in addition to the objective formulation and the adopted optimisation strategy (Section 2.3). We demonstrate the efficacy of the proposed objective formulation with two examples (one for the unimodal and one for pentamodal metamaterial) in Section 3. The obtained optimised metamaterials are then subjected to a geometrically nonlinear analysis, and our findings are summarised in Section 5.

2 Methodology

2.1 Numerical model

Assuming the metamaterial as a three-dimensional periodic truss structure allowed us to investigate the response of a Periodic Unit Cell (PUC) as its Representative Volume Element. We modelled the PUC with a ground structure containing discrete 3D trusses with predefined positions and orientations as shown in Fig. 2.1. As the shape of cross sections does not affect the stiffness of the truss structure, we assumed circular cross sections with area a_e for each truss rod e as the primal unknowns for optimisation. All cross-sectional areas a_e are collectively stored in a vector \mathbf{a} .

To determine the mechanical response of the PUC, we used a linear truss model, governed by the global stiffness matrix $\mathbf{K}(\mathbf{a})$ assembled from the local contributions of individual rods such that formally

$$\mathbf{K}(\mathbf{a}) = \sum_e \mathbf{L}_e^T \mathbf{T}_e^T \mathbf{K}_e^\ell(a_e) \mathbf{T}_e \mathbf{L}_e, \quad (2.1)$$

where \mathbf{L}_e denotes Boolean localisation matrices, \mathbf{T}_e is a transformation matrix containing directional cosines of the e -th rod, and the element stiffness matrix \mathbf{K}_e^ℓ in the local coordinate system reads as

$$\mathbf{K}_e^\ell(a_e) = \frac{Ea_e}{L_e} \begin{bmatrix} 1 & -1 \\ -1 & 1 \end{bmatrix}, \quad (2.2)$$

where E stands for Young's modulus and L_e refers to the initial length of the e -th rod.

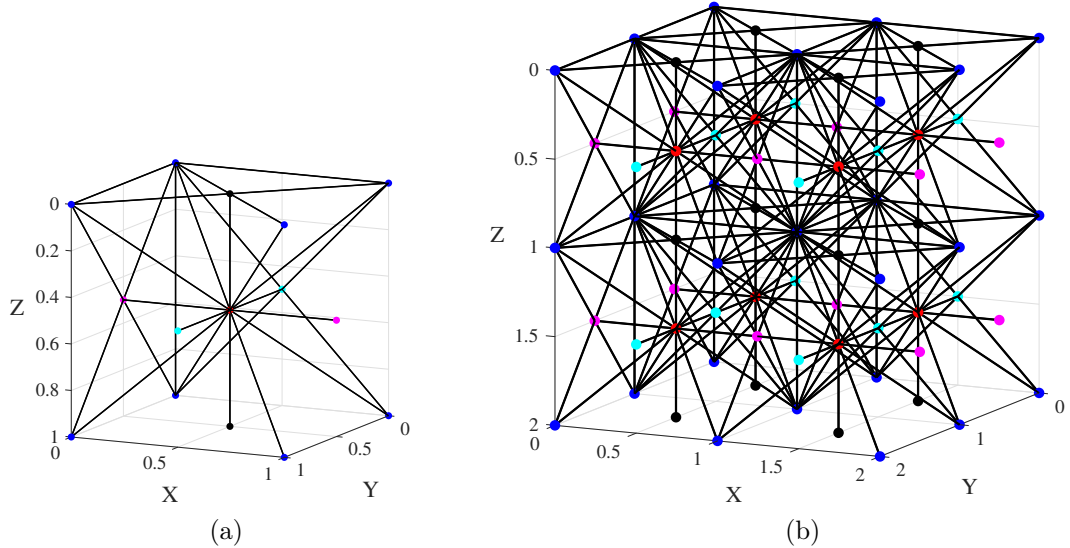


Figure 2.1: Two periodic ground structures considered in the study: (a) smaller ground structure with dimensions of $1 \times 1 \times 1$, and (b) larger ground structure with dimensions of $2 \times 2 \times 2$.

2.2 First-order homogenisation

The homogenisation determines the effective response of a heterogeneous PUC as if it were an equivalent homogeneous material point subjected to the same uniform strain field \mathbf{E} . For the linear problem considered here, the homogenised response is captured by the effective stiffness matrix $\mathbf{D}^{\text{hom}}(\mathbf{a})$.

In our study, we employed the first order numerical homogenisation [26] to obtain the effective properties of the metamaterial. The total displacement field $\tilde{\mathbf{u}}(\tilde{\mathbf{x}})$ was thus assumed in the form

$$\tilde{\mathbf{u}}(\tilde{\mathbf{x}}) = \tilde{\mathbf{u}}^{\mathbf{E}}(\tilde{\mathbf{x}}) + \tilde{\mathbf{u}}^*(\tilde{\mathbf{x}}), \quad (2.3)$$

where $\tilde{\mathbf{u}}^{\mathbf{E}}$ denotes the macroscopic part of the displacement field and $\tilde{\mathbf{u}}^*$ is the fluctuation field caused by the heterogeneity of the metamaterial [27].

For the discrete system, degrees of freedom (DOFs) related to the macroscopic displacement of the j -th node are coupled to the vectorial representation of the symmetric second-order tensor \mathbf{E} (using the engineering notation) via matrix \mathbf{Q}_j containing coordinates of node j ,

$$\mathbf{u}_j^{\mathbf{E}} = \begin{bmatrix} x_j & 0 & 0 & 0 & \frac{1}{2}z_j & \frac{1}{2}y_j \\ 0 & y_j & 0 & \frac{1}{2}z_j & 0 & \frac{1}{2}x_j \\ 0 & 0 & z_j & \frac{1}{2}y_j & \frac{1}{2}x_j & 0 \end{bmatrix} \mathbf{E} = \mathbf{Q}_j \mathbf{E}. \quad (2.4)$$

The displacement degrees of freedom \mathbf{u} , including both the macroscopic and fluctuation part, then follow as

$$\mathbf{u} = \begin{bmatrix} \mathbf{Q} & \mathbf{I} \end{bmatrix} \begin{bmatrix} \mathbf{E} \\ \mathbf{u}^* \end{bmatrix} = \widehat{\mathbf{Q}} \widehat{\mathbf{u}}, \quad (2.5)$$

where \mathbf{Q} contains vertically concatenated contributions \mathbf{Q}_j , \mathbf{I} stands for the identity matrix, and \mathbf{u}^* denotes the fluctuation DOFs. Due to the assumed periodic boundary conditions, not all DOFs in \mathbf{u}^* are independent. Accounting for the periodic source-image pairs and preventing rigid body motions by setting zero fluctuation at one selected node, the fluctuation DOFs can be expressed in terms of a subset of unknowns v ,

$$\widehat{\mathbf{u}} = \begin{bmatrix} \mathbf{E} \\ \mathbf{u}^* \end{bmatrix} = \begin{bmatrix} \mathbf{I} & \mathbf{0} \\ \mathbf{0} & \mathbf{P} \end{bmatrix} \begin{bmatrix} \mathbf{E} \\ v \end{bmatrix} = \widehat{\mathbf{P}} \widehat{v}, \quad (2.6)$$

with \mathbf{P} being a Boolean matrix facilitating the periodic boundary conditions.

Combining the discrete first-order displacement decomposition (2.5) and periodicity enforcement (2.6), the strain energy of a PUC model can be expressed as

$$\begin{aligned} \mathcal{E}(\mathbf{E}, v) &= \frac{1}{2} \widehat{v}^{\text{T}} \widehat{\mathbf{P}}^{\text{T}} \widehat{\mathbf{Q}}^{\text{T}} \mathbf{K}(\mathbf{a}) \widehat{\mathbf{Q}} \widehat{\mathbf{P}} \widehat{v} \\ &= \frac{1}{2} \begin{bmatrix} \mathbf{E} \\ v \end{bmatrix}^{\text{T}} \begin{bmatrix} \mathbf{Q}^{\text{T}} \mathbf{K}(\mathbf{a}) \mathbf{Q} & \mathbf{Q}^{\text{T}} \mathbf{K}(\mathbf{a}) \mathbf{P} \\ \mathbf{P}^{\text{T}} \mathbf{K}(\mathbf{a}) \mathbf{Q} & \mathbf{P}^{\text{T}} \mathbf{K}(\mathbf{a}) \mathbf{P} \end{bmatrix} \begin{bmatrix} \mathbf{E} \\ v \end{bmatrix} \\ &= \frac{1}{2} \begin{bmatrix} \mathbf{E} \\ v \end{bmatrix}^{\text{T}} \begin{bmatrix} \widehat{\mathbf{K}}_{\mathbf{E}\mathbf{E}}(\mathbf{a}) & \widehat{\mathbf{K}}_{\mathbf{E}v}(\mathbf{a}) \\ \widehat{\mathbf{K}}_{v\mathbf{E}}(\mathbf{a}) & \widehat{\mathbf{K}}_{vv}(\mathbf{a}) \end{bmatrix} \begin{bmatrix} \mathbf{E} \\ v \end{bmatrix}. \end{aligned} \quad (2.7)$$

From the homogenisation perspective, v can be treated as internal unknowns, which can be uniquely solved for a prescribed \mathbf{E} , leaving us with the condensed form

$$\tilde{\mathcal{E}}(\mathbf{E}) = \frac{1}{2} \mathbf{E}^{\text{T}} \left(\widehat{\mathbf{K}}_{\mathbf{E}\mathbf{E}}(\mathbf{a}) - \widehat{\mathbf{K}}_{\mathbf{E}v}(\mathbf{a}) \widehat{\mathbf{K}}_{vv}^{-1}(\mathbf{a}) \widehat{\mathbf{K}}_{v\mathbf{E}}(\mathbf{a}) \right) \mathbf{E} = \frac{1}{2} \mathbf{E}^{\text{T}} \mathbf{K}^{\text{eff}}(\mathbf{a}) \mathbf{E}. \quad (2.8)$$

Comparing the last row of (2.8) with an expression for the strain energy stored in a homogeneous material of volume V subjected to \mathbf{E} yields the final formula for the effective stiffness matrix

$$\mathbf{D}^{\text{hom}}(\mathbf{a}) = \frac{1}{V} \mathbf{K}^{\text{eff}}(\mathbf{a}). \quad (2.9)$$

For a detailed exposition and discussion of the adopted homogenisation scheme, we kindly refer the reader to our previous work [28].

2.3 Topology optimisation

To optimise the structure of multimodal metamaterials, we utilised the inverse homogenisation [18] with an objective function \mathcal{O} comprising a ratio between a projected stiffness α , defined via a unit modal deformation \mathbf{p} as

$$\alpha(\mathbf{a}) = \mathbf{p}^T \mathbf{D}^{\text{hom}}(\mathbf{a}) \mathbf{p}, \quad (2.10)$$

and k -th largest eigenvalue λ_k of a residual stiffness matrix \mathbf{D}^{res} obtained by subtracting the contribution of the projected stiffness α , i.e.

$$\mathbf{D}^{\text{res}}(\mathbf{a}) = \mathbf{D}^{\text{hom}}(\mathbf{a}) - \alpha(\mathbf{a}) \mathbf{p} \mathbf{p}^T. \quad (2.11)$$

In particular, the objective function for a unimodal metamaterial contains the fifth largest eigenvalue (out of six) of \mathbf{D}^{res} , as its goal is to maximise the gap between the compliant mode pertinent to α and the second smallest stiffness eigenvalue (the smallest eigenvalue of \mathbf{D}^{res} is zero by definition),

$$\mathcal{O}^{\text{I}}(\mathbf{a}) = \frac{\lambda_5(\mathbf{a})}{\alpha^{\text{I}}(\mathbf{a})}, \quad (2.12)$$

while the objective function for a pentamodal material includes the largest eigenvalue,

$$\mathcal{O}^{\text{V}}(\mathbf{a}) = \frac{\alpha^{\text{V}}(\mathbf{a})}{\lambda_1(\mathbf{a})}, \quad (2.13)$$

because all other stiffness components shall vanish compared to the stiffness α^{V} in a predefined mode \mathbf{p} .

This objective function is volume independent as both α and λ scale linearly with the linear scaling of \mathbf{a} , and thus no additional volume constraint is needed. Formally, our optimisation problem reads

$$\max_{\mathbf{a}} \mathcal{O}^{\bullet}(\mathbf{a}) \quad (2.14)$$

$$\underline{a} \leq a_e \leq \bar{a}, \quad (2.15)$$

where we set the upper bound \bar{a} such that the diameter of the largest circular cross-section is at maximum one tenth of the shortest truss rod in the ground structure, and the lower bound $\underline{a} = 10^{-4} \cdot \bar{a}$ is posed to avoid an ill-conditioned system in homogenisation (2.8).

Despite a seemingly complex structure of the objective, a gradient with respect to the design variables \mathbf{a} is readily available via the chain rule, i.e.

$$\frac{\partial}{\partial a_e} \mathcal{O}^{\text{I}}(\mathbf{a}) = \frac{\frac{\partial \lambda_5(\mathbf{a})}{\partial a_e} \alpha^{\text{I}}(\mathbf{a}) - \frac{\partial \alpha^{\text{I}}(\mathbf{a})}{\partial a_e} \lambda_5(\mathbf{a})}{\alpha^{\text{I}^2}(\mathbf{a})} \quad (2.16)$$

and

$$\frac{\partial}{\partial a_e} \mathcal{O}^V(\mathbf{a}) = \frac{\frac{\partial \alpha^V(\mathbf{a})}{\partial a_e} \lambda_1(\mathbf{a}) - \frac{\partial \lambda_1(\mathbf{a})}{\partial a_e} \alpha^V(\mathbf{a})}{\lambda_1^2(\mathbf{a})}, \quad (2.17)$$

respectively.

The sensitivity of the projected stiffness α with a given \mathbf{p} follows directly from the definition (2.10)

$$\frac{\partial \alpha(\mathbf{a})}{\partial a_e} = \mathbf{p}^\top \frac{\partial \mathbf{D}^{\text{hom}}(\mathbf{a})}{\partial a_e} \mathbf{p}. \quad (2.18)$$

A similar expression also holds for the sensitivity of the k -th largest eigenvalue, that is

$$\frac{\partial \lambda_k(\mathbf{a})}{\partial a_e} = \mathbf{v}_k^\top \frac{\partial \mathbf{D}^{\text{res}}(\mathbf{a})}{\partial a_e} \mathbf{v}_k, \quad (2.19)$$

where \mathbf{v}_k is the eigenvector pertinent to the k -th largest eigenvalue and

$$\frac{\partial \mathbf{D}^{\text{res}}(\mathbf{a})}{\partial a_e} = \frac{\partial \mathbf{D}^{\text{hom}}(\mathbf{a})}{\partial a_e} - \frac{\partial \alpha(\mathbf{a})}{\partial a_e} \mathbf{p} \mathbf{p}^\top. \quad (2.20)$$

The last missing link in the chain rule is the sensitivity of the effective stiffness matrix

$$\frac{\partial \mathbf{D}^{\text{hom}}(\mathbf{a})}{\partial a_e} = \frac{1}{V} \frac{\partial \mathbf{K}^{\text{eff}}(\mathbf{a})}{\partial a_e} = \frac{1}{V} \frac{\partial}{\partial a_e} \left(\widehat{\mathbf{K}}_{EE}(\mathbf{a}) - \widehat{\mathbf{K}}_{Ev}(\mathbf{a}) [\widehat{\mathbf{K}}_{vv}(\mathbf{a})]^{-1} \widehat{\mathbf{K}}_{vE}(\mathbf{a}) \right). \quad (2.21)$$

Dropping the explicit dependence on \mathbf{a} and using the terse notation $\widehat{\mathbf{K}}_{\bullet\bullet, a_e}$ for the partial derivative with respect to a_e , we obtain

$$\begin{aligned} \frac{\partial \mathbf{K}^{\text{eff}}}{\partial a_e} &= \widehat{\mathbf{K}}_{EE, a_e} - \widehat{\mathbf{K}}_{Ev, a_e} \widehat{\mathbf{K}}_{vv}^{-1} \widehat{\mathbf{K}}_{vE} + \widehat{\mathbf{K}}_{Ev} \widehat{\mathbf{K}}_{vv}^{-1} \widehat{\mathbf{K}}_{vv, a_e} \widehat{\mathbf{K}}_{vv}^{-1} \widehat{\mathbf{K}}_{vE} - \widehat{\mathbf{K}}_{Ev} \widehat{\mathbf{K}}_{vv}^{-1} \widehat{\mathbf{K}}_{vE, a_e} \\ &= \widehat{\mathbf{K}}_{EE, a_e} - \widehat{\mathbf{K}}_{Ev, a_e} \Theta + \Theta^\top \widehat{\mathbf{K}}_{vv, a_e} \Theta - \Theta^\top \widehat{\mathbf{K}}_{vE, a_e}, \end{aligned} \quad (2.22)$$

where Θ is the solution to an adjoint problem

$$\widehat{\mathbf{K}}_{vv} \Theta = \widehat{\mathbf{K}}_{vE}. \quad (2.23)$$

The sensitivities of the four sub-blocks $\widehat{\mathbf{K}}_{EE}$, $\widehat{\mathbf{K}}_{Ev}$, $\widehat{\mathbf{K}}_{vE}$, and $\widehat{\mathbf{K}}_{vv}$ follow the same pattern as they are (potentially asymmetric) projections of $\mathbf{K}(\mathbf{a})$, recall (2.7), and thus they all require only

$$\frac{\partial \mathbf{K}(\mathbf{a})}{\partial a_e} = \mathbf{L}_e^\top \mathbf{T}_e^\top \frac{E}{L_e} \begin{bmatrix} 1 & -1 \\ -1 & 1 \end{bmatrix} \mathbf{T}_e \mathbf{L}_e. \quad (2.24)$$

Being able to express the gradient of the objective function analytically led us to the adoption of a steepest ascent method. To compensate for the fact that we did not compute a Hessian, we supplemented the steepest ascent method with the line search method equipped with the Armijo rule [29].

We started by randomly initialising feasible design variables \mathbf{a} that satisfy the box constraints (2.15). In each iteration, we first calculated the gradient of the objective function $\nabla \mathcal{O}$ using the expressions introduced above. Next, we defined a modified gradient $\widehat{\nabla \mathcal{O}}(\mathbf{a})$ by projecting the original one on the active box constraints such that

$$\widehat{\nabla \mathcal{O}}_e(\mathbf{a}) = \begin{cases} 0 & \text{if } \mathbf{a}_e = \bar{a} \wedge \nabla \mathcal{O}_e(\mathbf{a}) > 0 \\ 0 & \text{if } \mathbf{a}_e = \underline{a} \wedge \nabla \mathcal{O}_e(\mathbf{a}) < 0 \\ \nabla \mathcal{O}_e(\mathbf{a}) & \text{otherwise.} \end{cases} \quad (2.25)$$

The modified gradient then constituted the search direction for the inexact one-dimensional maximisation in the current iteration. Starting with an initial step length computed as the minimum of candidate lengths $\tilde{\nu}_e$ ensuring that the box constraints are not violated in the new state, i.e.,

$$\tilde{\nu}_e = \begin{cases} (\bar{a} - \mathbf{a}_e) / \widehat{\nabla \mathcal{O}_e(\mathbf{a})} & \text{if } \widehat{\nabla \mathcal{O}_e(\mathbf{a})} > 0 \\ (\underline{a} - \mathbf{a}_e) / \widehat{\nabla \mathcal{O}_e(\mathbf{a})} & \text{if } \widehat{\nabla \mathcal{O}_e(\mathbf{a})} < 0 \\ 0 & \text{otherwise,} \end{cases} \quad (2.26)$$

we halved the step length until a significant objective increase is achieved in terms of the Armijo rule with coefficient c_1 set to 0.1. We iterated until both the relative change in design variables and the relative change in the objective value dropped below $\epsilon = 10^{-6}$. The structure of the adopted optimisation strategy is summarised in Algorithm 1.

Algorithm 1 Adopted optimisation strategy

Randomly initialise \mathbf{a}_0 ; $i = 0$
repeat
 compute $\nabla \mathcal{O}(\mathbf{a}_i)$
 $\widehat{\nabla \mathcal{O}}(\mathbf{a}_i) = \mathbf{modify} \nabla \mathcal{O}(\mathbf{a}_i)$
 compute $\tilde{\nu}$
 $\nu = \min(\tilde{\nu})$
 repeat
 $\mathbf{a}_{new} = \mathbf{a} + \nu \widehat{\nabla \mathcal{O}}(\mathbf{a}_i)$
 $\nu = \nu / 2$
 until $\mathcal{O}(\mathbf{a}_i + \nu \widehat{\nabla \mathcal{O}}) \geq \mathcal{O}(\mathbf{a}_i) + c_1 \nu \widehat{\nabla \mathcal{O}}(\mathbf{a}_i)^\top \widehat{\nabla \mathcal{O}}(\mathbf{a}_i)$
 $i = i + 1$
 $\mathbf{a}_i = \mathbf{a}_{new}$
end
until $\|\mathbf{a}_i - \mathbf{a}_{i-1}\| / \|\mathbf{a}_i\| < \epsilon \wedge \|\mathcal{O}(\mathbf{a}_i) - \mathcal{O}(\mathbf{a}_{i-1})\| / \|\mathcal{O}(\mathbf{a}_i)\| < \epsilon$

3 Optimised metamaterials

We demonstrate the proposed objective formulation with two optimisation problems: unimodal and pentamodal metamaterials. As stated in the previous section, both optimisation problems share the same formulation but differ in the definition of the objective function; recall Eqs. (2.12) and (2.13). In addition, we show the results for two ground structures depicted in Fig. 2.1, with the larger ground structure being a periodic extension of the smaller one. In all cases, we assumed Young’s modulus of elasticity $E = 1$. Since the response of the metamaterial model is linear in E , the homogenised stiffness matrices can be understood as normalised with respect to E .

3.1 Unimodal metamaterial

We start with optimising the microstructure of a unimodal metamaterial with vanishing shear modulus in the yz direction. To this end, we set

$$\mathbf{p} = [0 \ 0 \ 0 \ 1 \ 0 \ 0]^T$$

in the objective definition (2.12).

Since the whole problem is non-convex, the gradient method renders only local optima. Consequently, the optimised microstructure depends on the initial distribution of cross-sectional areas \mathbf{a}_0 . The best results obtained out of 100 independent starting points \mathbf{a}_0 are shown in Fig. 3.1 for both ground structures, with the line thicknesses indicating the size of the cross-sectional areas.

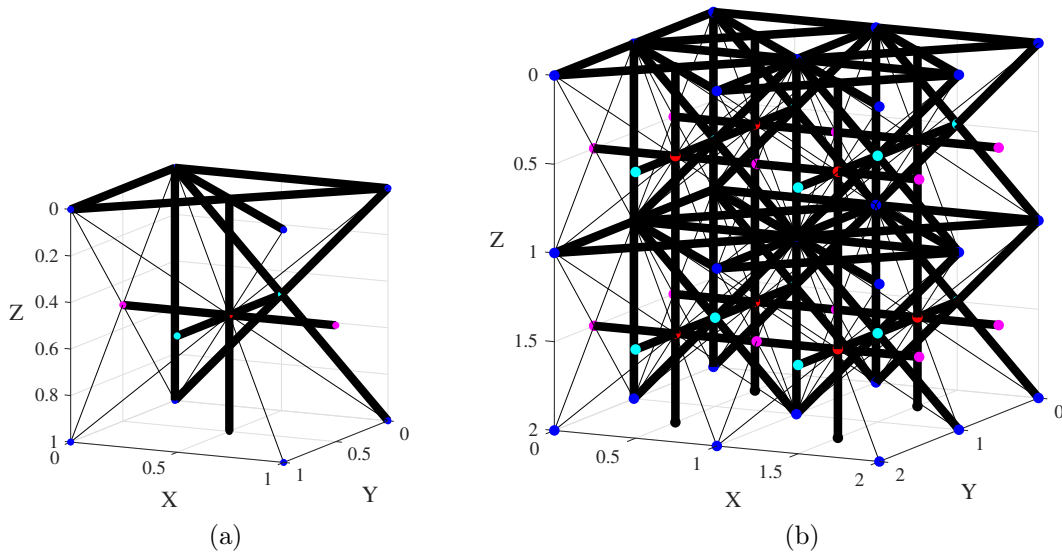


Figure 3.1: Optimised smaller (a) and larger (b) PUCs of a pentamodal metamaterial with maximised shear modulus in the yz plane.

The homogenised matrix $D^{\text{hom}}(\mathbf{a}_{\text{opt}})$ of both optimised structures took the form

$$D^{\text{hom}} = \begin{bmatrix} 6.70 & 1.39 & 1.39 & 0.00 & 0.00 & 0.00 \\ 1.39 & 5.32 & 0.00 & 0.00 & 0.00 & 0.00 \\ 1.39 & 0.00 & 5.32 & 0.00 & 0.00 & 0.00 \\ 0.00 & 0.00 & 0.00 & 0.00 & 0.00 & 0.00 \\ 0.00 & 0.00 & 0.00 & 0.00 & 1.39 & 0.00 \\ 0.00 & 0.00 & 0.00 & 0.00 & 0.00 & 1.39 \end{bmatrix} \times 10^{-3}, \quad (3.1)$$

and exhibited almost zero value at the position $D_{4,4}^{\text{hom}}$. The value of the associated objective function was 4.79×10^3 .

The best result obtained for the larger ground structure converged to a geometry that is a periodic extension of the best result obtained for the smaller ground structure, i.e. the larger ground structure comprises eight PUCs. Furthermore, we subsequently tested the optimisation of unimodal metamaterial for vanishing shear modules in the xz ($\mathbf{p} = [0 \ 0 \ 0 \ 0 \ 1 \ 0]^T$) and xy ($\mathbf{p} = [0 \ 0 \ 0 \ 0 \ 0 \ 1]^T$) planes. The optimised structures for these scenarios are rotated versions of the metamaterial with a minimised shear modulus in the yz direction, as shown in Fig. 3.2. The corresponding homogenised matrices are—up to a small numerical difference—only permutations of (3.1). These observations indicate a strong local optimum for such a design, corroborated further by the fact that the same design was achieved for the majority of independent runs with random initial distribution of truss cross-sectional areas.

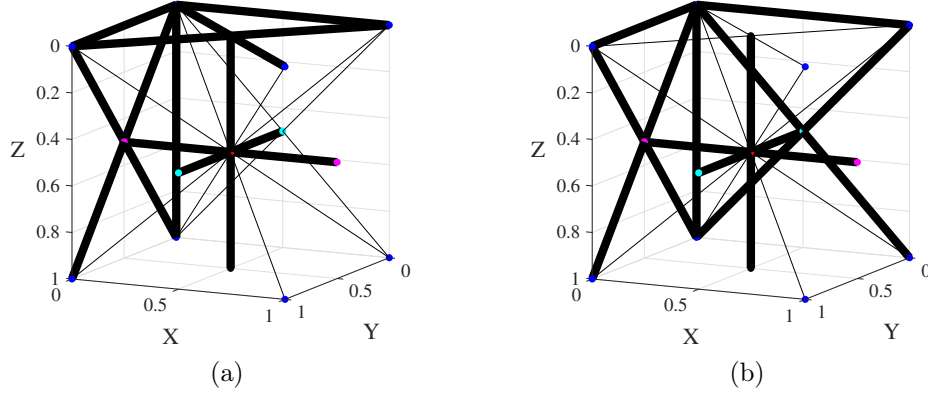


Figure 3.2: Optimised PUCs of unimodal metamaterials with minimised shear modulus in the xz (a) and xy (b) plane.

3.2 Pentamodal metamaterial

As the second example, we optimised the same ground structures for a meta-fluid behaviour, using the objective definition (2.13) with

$$\mathbf{p} = \left[\frac{1}{\sqrt{3}} \quad \frac{1}{\sqrt{3}} \quad \frac{1}{\sqrt{3}} \quad 0 \quad 0 \quad 0 \right]^T.$$

This objective proved to be more challenging than its unimodal counterpart, as there was no strong local optimum. Different optimisation runs with different initial states thus yielded distinct results with suboptimal performance compared to the existing pentamodal design of Milton and Cherkaev [3], which was attainable with the ground structures we chose.

A common remedy to suppress the sensitivity to local minima widely used in the community of structural optimisation is to use a separable local approximation such as the method of moving asymptotes [30]. Here, we adopted a different strategy that built on sequential 1D minimisation problems along individual design variables. This approach fits in the provided Algorithm 1 by introducing a gradient modification.

In each iteration, we randomly select a single design variable and compute the modified gradient specifically for that variable. If the modified gradient is non-zero, we perform a 1D line search while maintaining the values of the other design variables constant. If the modified gradient equals zero, we proceed to the subsequent iteration, iterating through the randomly selected design variables until the optimised structure is achieved. Clearly, such a modification results in an increase in iterations. However, with this method, the optimisation yielded a design that corresponded to the design by Milton and Cherkaev [3]. To ensure that the majority of individual optimisation runs will yield the mentioned design, the maximum values of the initial variables must be smaller than $\bar{a}/10$. In particular, optimisation with smaller values of initial variables tends to result in a higher objective function value than optimisation using larger ones.

The best obtained PUCs of the pentamodal material are shown in Fig. 3.3. Similarly to the unimodal metamaterial, the larger PUC converges towards a geometry composed of eight smaller identical PUCs. For completeness, we list the homogenised matrix \mathbf{D}^{hom}

$$\mathbf{D}^{\text{hom}} = \begin{bmatrix} 7.56 & 7.56 & 7.56 & 0.00 & 0.00 & 0.00 \\ 7.56 & 7.56 & 7.56 & 0.00 & 0.00 & 0.00 \\ 7.56 & 7.56 & 7.56 & 0.00 & 0.00 & 0.00 \\ 0.00 & 0.00 & 0.00 & 0.00 & 0.00 & 0.00 \\ 0.00 & 0.00 & 0.00 & 0.00 & 0.00 & 0.00 \\ 0.00 & 0.00 & 0.00 & 0.00 & 0.00 & 0.00 \end{bmatrix} \times 10^{-4}, \quad (3.2)$$

with objective function achieving a value of 4.27×10^3 . Note that the result for the $2 \times 2 \times 2$ ground structure features two interconnected networks and thus its homogenised response is twice as stiff compared to the stiffness of the classical metafluid structure shown in Fig. 1.1.

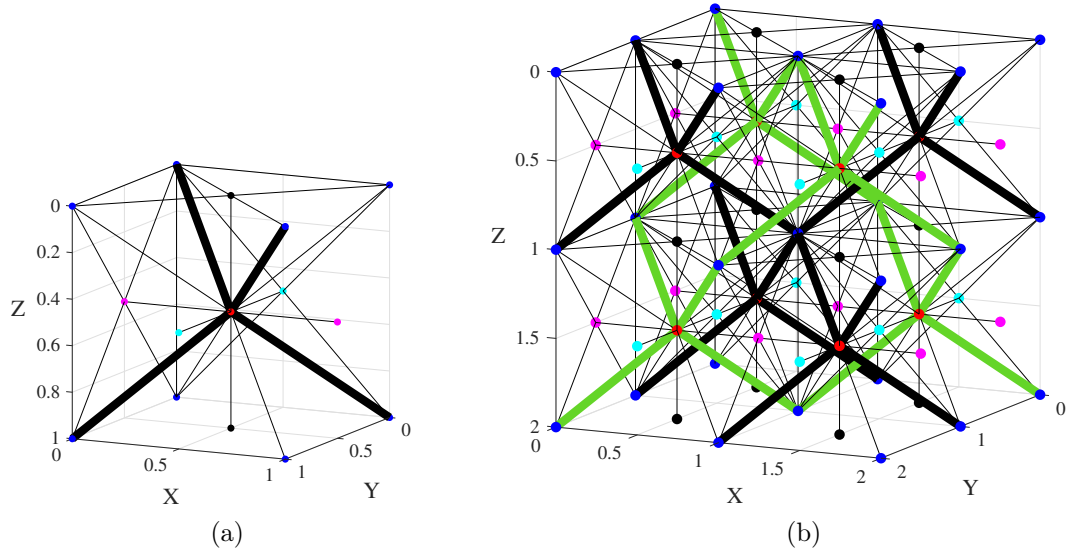


Figure 3.3: Optimised smaller (a) and larger (b) PUCs of a pentamodal metamaterial with maximised bulk modulus. The larger PUC of the pentamodal metamaterial consists of two independent structures (plotted in black and green).

4 Geometrically nonlinear analysis

Up to this point, we have assumed a linear elastic response of metamaterial PUCs. However, the optimised metamaterials presented in the previous section exhibit in some way unusual behaviour under external loading, prompting the question whether similar modal characteristics persist in the deformed state. To investigate this, we introduce a geometrically nonlinear model in the following sections, which enables the prediction of metamaterial behaviour under large deformations.

The key difference between the linear elastic and geometrically nonlinear models lies in the fact that the linear model considers only the initial configuration of the structure, whereas the nonlinear model evaluates its response in the current, deformed state. In the geometrically nonlinear approach, the nodal positions are updated after deformation, which directly affects elements lengths and their stiffnesses. However, both models still assume material linearity.

4.1 Numerical model

Since the optimised metamaterials were modelled as truss structures, the derivation of geometrically nonlinear model is outlined here only for truss elements. The total energy $\mathcal{E}(\mathbf{u})$ of the model can be defined as the sum of the internal $\mathcal{E}_{\text{int}}(\mathbf{u})$ and external $\mathcal{E}_{\text{ext}}(\mathbf{u})$ energy, written as

$$\mathcal{E}(\mathbf{u}) = \mathcal{E}_{\text{int}}(\mathbf{u}) - \mathcal{E}_{\text{ext}}(\mathbf{u}), \quad (4.1)$$

where the external energy \mathcal{E}_{ext} is defined in terms of external loading \mathbf{F}_{ext} and nodal displacements \mathbf{u} as

$$\mathcal{E}_{\text{ext}}(\mathbf{u}) = \mathbf{F}_{\text{ext}} \mathbf{u}. \quad (4.2)$$

The internal energy $\mathcal{E}_{\text{int}}(\mathbf{u})$ of a geometrically nonlinear system is expressed as the sum of the energies of all n elements in the PUC, written as

$$\mathcal{E}_{\text{int}}(\mathbf{u}) = \sum_{e=1}^n \mathcal{E}_{\text{int}}^e(\mathbf{u}), \quad (4.3)$$

where the contribution of the e -th element takes the form

$$\mathcal{E}_{\text{int}}^e(\mathbf{u}) = \frac{1}{2} \frac{Ea_e}{L_e} \Delta l_e^2(\mathbf{u}). \quad (4.4)$$

Here, the geometrical nonlinearity arises from the term $\Delta l_e(\mathbf{u})$, which represents the difference between the deformed rod length $l_e(\mathbf{u})$ and its initial (undeformed) length L_e , and is defined as

$$\Delta l_e(\mathbf{u}) = l_e(\mathbf{u}) - L_e. \quad (4.5)$$

This formulation follows the Total Lagrangian method, which incrementally accounts for deformations relative to the initial configuration. An alternative is the Updated Lagrangian approach, where deformations are measured relative to the previous configuration [31]. In this work, the Total Lagrangian method is used as it is suitable for truss structures.

The length $l_e(\mathbf{u})$ of the rod after deformation depends on the nodal displacements explicitly as

$$l_e(\mathbf{u}) = \sqrt{\Delta x_e^2(\mathbf{u}) + \Delta y_e^2(\mathbf{u}) + \Delta z_e^2(\mathbf{u})}, \quad (4.6)$$

where the differences in the spatial coordinates between beginning (B) and end (E) node are defined as

$$\begin{aligned}\Delta x_e(\mathbf{u}) &= (x_E + u_E) - (x_B + u_B) \\ \Delta y_e(\mathbf{u}) &= (y_E + v_E) - (y_B + v_B) \\ \Delta z_e(\mathbf{u}) &= (z_E + w_E) - (z_B + w_B),\end{aligned}\tag{4.7}$$

and collected in the variable $\mathbf{s}(\mathbf{u})$ for use in subsequent derivations

$$\mathbf{s}_e(\mathbf{u}) = [\Delta x_e(\mathbf{u}) \quad \Delta y_e(\mathbf{u}) \quad \Delta z_e(\mathbf{u})].\tag{4.8}$$

4.1.1 Residual vector

The residual vector $\mathbf{R}(\mathbf{u})$ is the first-order derivative of PUC's energy $\mathcal{E}(\mathbf{u})$, defined in Eq. (4.1)

$$\mathbf{R}(\mathbf{u}) = \frac{\partial \mathcal{E}(\mathbf{u})}{\partial \mathbf{u}} = \frac{\partial \mathcal{E}_{\text{int}}(\mathbf{u})}{\partial \mathbf{u}} + \frac{\partial \mathcal{E}_{\text{ext}}(\mathbf{u})}{\partial \mathbf{u}},\tag{4.9}$$

where the individual components of \mathcal{E}_{int} are specified in Eqs. (4.3, 4.4), and those of \mathcal{E}_{ext} in Eq. (4.2). From Eq. (4.9) the residual vector $\mathbf{R}(\mathbf{u})$ can be easily written in the form

$$\mathbf{R}(\mathbf{u}) = \mathbf{F}_{\text{int}}(\mathbf{u}) - \mathbf{F}_{\text{ext}},\tag{4.10}$$

implying that the residual vector represents the imbalance between internal $\mathbf{F}_{\text{int}}(\mathbf{u})$ and external \mathbf{F}_{ext} forces at a given deformation state.

Since external forces \mathbf{F}_{ext} are directly defined by the prescribed loading, we only need to derive the internal forces $\mathbf{F}_{\text{int}}(\mathbf{u})$. To do so, we determine the derivative of the internal energy $\mathcal{E}_{\text{int}}(\mathbf{u})$ with respect to the nodal displacements \mathbf{u} , which for each truss element e reads as

$$\frac{\partial \mathcal{E}_{\text{int}}^e}{\partial u_j} = \frac{Ea_e}{L_e} \Delta l_e(\mathbf{u}) \frac{\partial \Delta l_e(\mathbf{u})}{\partial u_j},\tag{4.11}$$

where

$$\frac{\partial \Delta l_e(\mathbf{u})}{\partial u_j} = \frac{\partial l_e(\mathbf{u}) - L_e}{\partial u_j} = \frac{\partial l_e(\mathbf{u})}{\partial u_j}.\tag{4.12}$$

Applying the chain rule and using the Einstein summation rule, the sensitivity of the deformed rod's length $l_e(\mathbf{u})$ becomes

$$\frac{\partial l_e(\mathbf{u})}{\partial u_j} = \frac{\partial l_e(\mathbf{u})}{\partial \mathbf{s}_e(\mathbf{u})} \frac{\mathbf{s}_e(\mathbf{u})}{\partial u_j},\tag{4.13}$$

where $\mathbf{s}_e(\mathbf{u})$ represents differences in rod's spatial coordinates from Eq. (4.7). Evaluating this expression yields the sensitivity of the rod's length with respect to the nodal displacements u_e , which include only the displacements of the nodes belonging to the e -th element, as the residual vector of the e -th rod is sensitive only to them. It is derived as

$$\frac{\partial l_e(\mathbf{u})}{\partial u_e} = \left[-\frac{\Delta x_e(\mathbf{u})}{l_e(\mathbf{u})} \quad -\frac{\Delta y_e(\mathbf{u})}{l_e(\mathbf{u})} \quad -\frac{\Delta z_e(\mathbf{u})}{l_e(\mathbf{u})} \quad \frac{\Delta x_e(\mathbf{u})}{l_e(\mathbf{u})} \quad \frac{\Delta y_e(\mathbf{u})}{l_e(\mathbf{u})} \quad \frac{\Delta z_e(\mathbf{u})}{l_e(\mathbf{u})} \right]^T,\tag{4.14}$$

which can be expressed in terms of the directional cosines $\tilde{c}^e(\mathbf{u})$, grouped into the auxiliary variable $\vartheta_e(\mathbf{u})$ as

$$\frac{\partial l_e(\mathbf{u})}{\partial u_e} = [-\tilde{c}_x^e(\mathbf{u}) \quad -\tilde{c}_y^e(\mathbf{u}) \quad -\tilde{c}_z^e(\mathbf{u}) \quad \tilde{c}_x^e(\mathbf{u}) \quad \tilde{c}_y^e(\mathbf{u}) \quad \tilde{c}_z^e(\mathbf{u})]^T = \vartheta_e(\mathbf{u}).\tag{4.15}$$

Substituting into Eq. (4.9), the vector of internal forces $\mathbf{F}_{\text{int}}^e$ for the e -th rod is obtained as

$$\mathbf{F}_{\text{int}}^e(\mathbf{u}) = \frac{Ea_e}{L_e} \Delta l_e(\mathbf{u}) \vartheta_e(\mathbf{u}), \quad (4.16)$$

which can be simplified for further derivations as

$$\mathbf{F}_{\text{int}}^e(\mathbf{u}) = N_e(\mathbf{u}) \vartheta_e(\mathbf{u}). \quad (4.17)$$

Taking this into account and recalling the definition of the residual vector $\mathbf{R}(\mathbf{u})$ from Eq. (4.10), the residual vector takes the form

$$\mathbf{R}_e(\mathbf{u}) = N_e(\mathbf{u}) \vartheta_e(\mathbf{u}) - \mathbf{F}_{\text{ext}}^e. \quad (4.18)$$

4.1.2 Stiffness matrix

The tangent stiffness matrix $\mathbf{K}(\mathbf{u})$ is defined as the second-order derivative of the PUC's energy

$$\mathbf{K}_{jk}(\mathbf{u}) = \frac{\partial \mathcal{E}(\mathbf{u})}{\partial u_j \partial u_k}, \quad (4.19)$$

therefore it can be obtained from the residual vector $\mathbf{R}(\mathbf{u})$ as

$$\mathbf{K}_{jk}^e(\mathbf{u}) = \frac{\partial \mathbf{R}_j^e(\mathbf{u})}{\partial u_k}. \quad (4.20)$$

Since the external force term $\mathbf{F}_{\text{ext}}^e$ vanishes upon differentiating $\mathbf{R}^e(\mathbf{u})$ from Eq. (4.18), $\mathbf{K}^e(\mathbf{u})$ is directly derived from the vector of internal forces $\mathbf{F}_{\text{int}}^e(\mathbf{u})$, leading to

$$\mathbf{K}_{jk}^e(\mathbf{u}) = \frac{Ea_e}{L_e} \frac{\partial \Delta l_e(\mathbf{u}) \vartheta_j^e(\mathbf{u})}{\partial u_k}, \quad (4.21)$$

which can be further written as

$$\mathbf{K}_{jk}^e(\mathbf{u}) = \frac{Ea_e}{L_e} \left(\vartheta_j^e(\mathbf{u}) \frac{\partial \Delta l_e(\mathbf{u})}{\partial u_k} + \Delta l_e(\mathbf{u}) \frac{\partial \vartheta_j^e(\mathbf{u})}{\partial u_k} \right), \quad (4.22)$$

and corresponds to the sum of the material $\mathbf{K}_M(\mathbf{u})$ and the geometric $\mathbf{K}_G(\mathbf{u})$ stiffness matrix, such that

$$\mathbf{K}(\mathbf{u}) = \mathbf{K}_M(\mathbf{u}) + \mathbf{K}_G(\mathbf{u}). \quad (4.23)$$

The first term on the right-hand of Eq. (4.22) side has already been derived in Eqs. (4.12) - (4.15), resulting in

$$\vartheta_j^e(\mathbf{u}) \frac{\partial \Delta l_e(\mathbf{u})}{\partial u_k} = \vartheta_j^e(\mathbf{u}) \vartheta_k^{e\top}(\mathbf{u}), \quad (4.24)$$

which leads to the expression for the element material stiffness matrix $\mathbf{K}_{M,jk}^e(\mathbf{u})$ as

$$\mathbf{K}_{M,jk}^e(\mathbf{u}) = \frac{Ea_e}{L_e} \vartheta_j^e(\mathbf{u}) \vartheta_k^{e\top}(\mathbf{u}). \quad (4.25)$$

To compute the remaining term from Eq. (4.22), we first need to derive the sensitivity of directional cosines \tilde{c}^e , stored in the vector $\vartheta^e(\mathbf{u})$, with respect to the nodal displacement \mathbf{u} , defined as

$$\frac{\partial \vartheta_j^e(\mathbf{u})}{\partial u_k} = \frac{\partial}{\partial u_k} \frac{\mathbf{s}_e(\mathbf{u})}{l_e(\mathbf{u})}, \quad (4.26)$$

which can be further written in the form

$$\frac{\partial \vartheta_j^e(\mathbf{u})}{\partial u_k} = \frac{\frac{\partial s_e(\mathbf{u})}{\partial u_k} l_e(\mathbf{u}) - s_e(\mathbf{u}) \frac{\partial l_e(\mathbf{u})}{\partial u_k}}{l_e^2(\mathbf{u})}. \quad (4.27)$$

The sensitivities of $s_e(\mathbf{u})$ and $l_e(\mathbf{u})$ with respect to \mathbf{u}^e has already been used in Eq. (4.15). After defining the projection of the deformed length $l_e(\mathbf{u})$ onto given coordinate planes as

$$\begin{aligned} l_{yz}^e &= \sqrt{\Delta y_e^2(\mathbf{u}) + \Delta z_e^2(\mathbf{u})} \\ l_{xz}^e &= \sqrt{\Delta x_e^2(\mathbf{u}) + \Delta z_e^2(\mathbf{u})} \\ l_{xy}^e &= \sqrt{\Delta x_e^2(\mathbf{u}) + \Delta y_e^2(\mathbf{u})}, \end{aligned} \quad (4.28)$$

we can derive the geometric stiffness matrix $\mathbf{K}_{G,jk}^e(\mathbf{u})$ for e -th rod as

$$\mathbf{K}_G^e(\mathbf{u}) = \frac{Ea_e}{L_e} \frac{\Delta l_e(\mathbf{u})}{l_e^3(\mathbf{u})} \begin{bmatrix} l_{yz,i}^2 & -\Delta x_e \Delta y_e & -\Delta x_e \Delta z_e & -l_{yz,i}^2 & \Delta x_e \Delta y_e & \Delta x_e \Delta z_e \\ & l_{xz,i}^2 & -\Delta y_e \Delta z_e & \Delta x_e \Delta y_e & -l_{xz,i}^2 & \Delta y_e \Delta z_e \\ & & l_{xy,i}^2 & \Delta x_e \Delta z_e & \Delta y_e \delta z_e & -l_{xy,i}^2 \\ & \text{sym} & & l_{yz,i}^2 & -\Delta x_e \Delta y_e & -\Delta x_e \Delta z_e \\ & & & & l_{xz,i}^2 & -\Delta y_e \Delta z_e \\ & & & & & l_{xy,i}^2 \end{bmatrix}. \quad (4.29)$$

The geometrically nonlinear tangent stiffness matrix $\mathbf{K}_e(\mathbf{u})$ for e -th rod, defined in Eq. (4.23), is then expressed in terms of the material \mathbf{K}_M^e and the geometrical \mathbf{K}_G^e stiffness matrices from Eqs. (4.25), (4.29) in the form

$$\mathbf{K}_e(\mathbf{u}) = \frac{Ea_e}{L_e} \left(\vartheta_j^e(\mathbf{u}) \vartheta_k^e(\mathbf{u}) + \frac{\Delta l_e(\mathbf{u})}{l_e^3(\mathbf{u})} \tilde{\mathbf{K}}_G^e(\mathbf{u}) \right), \quad (4.30)$$

where $\tilde{\mathbf{K}}_G^e(\mathbf{u})$ corresponds to the symmetric matrix from Eq. (4.29).

4.2 Numerical strategy

To obtain the geometrically nonlinear response of the metamaterials subjected to external loading, we assume a displacement-controlled setup with prescribed macroscopic strain \mathbf{E} , that is incrementally increasing from $\mathbf{E} = 0$ to the final value $\widehat{\mathbf{E}}$ in pseudo-time loading steps.

In each loading step s , the macroscopic component of the nodal displacement $\mathbf{u}_s^{\mathbf{E}}$ was determined from the prescribed strain using the relation from Eq. (2.4). The increment to the fluctuation part of the displacement field is iteratively computed as a minimiser of the strain energy using the standard Newton algorithm, where the geometrically nonlinear stiffness matrix $\mathbf{K}(\mathbf{u}_k)$ serves as the Hessian and the residual vector $\mathbf{R}(\mathbf{u}_k)$ acts as the gradient.

This computed increment is then added to the fluctuation part of the displacement field from the previous iteration, denoted as \mathbf{u}_{k-1}^* . The full displacement field \mathbf{u}_{k+1} for the next iteration is then obtained as the sum of its macroscopic $\mathbf{u}_k^{\mathbf{E}}$ and fluctuation \mathbf{u}_k^* parts. The positions of the nodes are updated to model the geometrically nonlinear behaviour. These updated positions are then used for the following iteration, and once the convergence criteria are satisfied, they are used for the next loading step. The convergence criteria are defined such that there is no significant change in the computed displacement field and the internal and external forces are in equilibrium, as represented by the residual vector $\mathbf{R}(\mathbf{u}_k)$. The threshold for convergence was set to $\epsilon = 10^{-6}$. The entire procedure is summarised in Algorithm 2.

Algorithm 2 Geometrical nonlinearity

```

Initialise  $\mathbf{E}$  for loading steps
for each loading step
  compute  $\mathbf{u}_s^{\mathbf{E}}$ 
  repeat
    compute  $\mathbf{R}(\mathbf{u}_k), \mathbf{K}(\mathbf{u}_k)$ 
     $\Delta\mathbf{u}_k^* = -\mathbf{K}(\mathbf{u}_k)^{-1}\mathbf{R}(\mathbf{u}_k)$ 
     $\mathbf{u}_k^* = \mathbf{u}_{k-1}^* + \Delta\mathbf{u}_k^*$ 
     $\mathbf{u}_{k+1} = \mathbf{u}_s^{\mathbf{E}} + \mathbf{P}\mathbf{u}_k^*$ 
     $k = k + 1$ 
  until  $\|\Delta\mathbf{u}_k^*\| / \|\mathbf{u}_{k+1}\| > \epsilon \wedge \|\mathbf{R}(\mathbf{u}_k)\| > \epsilon$ 
end

```

4.3 Results

We computed the linear and nonlinear responses of the optimised unimodal metamaterial, shown in Fig. 3.1, and the pentamodal metamaterial from Fig. 3.3. The final value of the prescribed macroscopic strain was set to $\widehat{\mathbf{E}} = 0.3$ in one direction, with zero values in the remaining ones. The response of the PUCs was computed separately for all six principal directions. The results are shown in Fig. 4.1, where the dashed lines represent the linear response, and the solid lines of the corresponding colours show the geometrically nonlinear response. The responses more or less corresponds, and it can be observed that the optimised metamaterials retain their modality even under the maximum prescribed strain. Due to the symmetry of the metamaterials, the response of the PUC is identical in certain loading directions, as shown in Fig. 4.1.

The unimodal metamaterial, designed to minimise the shear modulus in the yz plane, requires significantly less energy to deform in this plane compared to the others, which was the goal of our optimisation. Similarly, from the response of the pentamodal metamaterial we can observe a visible gap between the shear and the bulk modulus, which can be deduced from the green lines corresponding to the loading along the x , y and z directions. This gap is characteristic of pentamodal metamaterials, as their only stiff mode of deformation is associated with the bulk modulus. Even though linear and geometrically nonlinear analysis results in similar response after loading in shear direction, closer look into selected loading curves in Fig. 4.2 shows a noticeable deviation between for both metamaterials, but energy values are quite small. Overall, both optimised metamaterials preserved their multimodal behaviour even under the maximum prescribed strain.

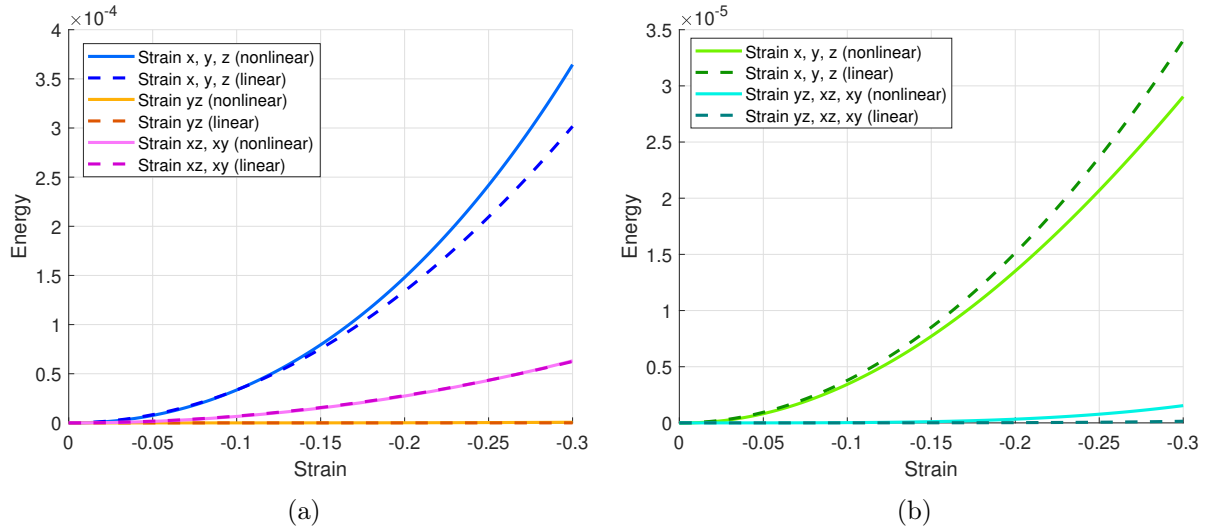


Figure 4.1: Comparison of strain-driven metamaterial response between the linear and geometrically nonlinear models for (a) unimodal metamaterial and (b) pentamodal metamaterial.

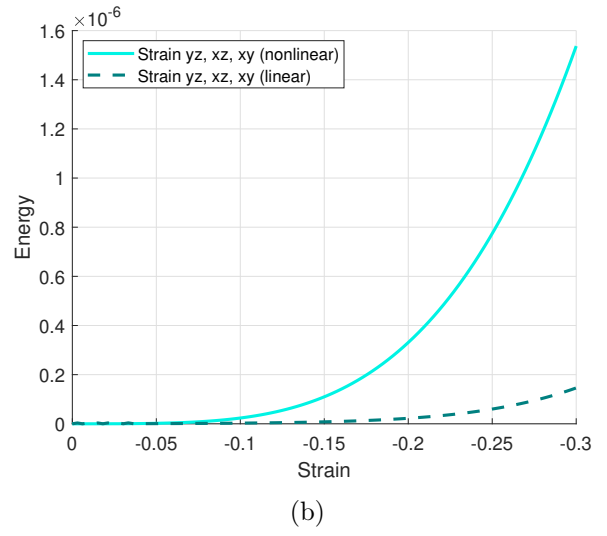
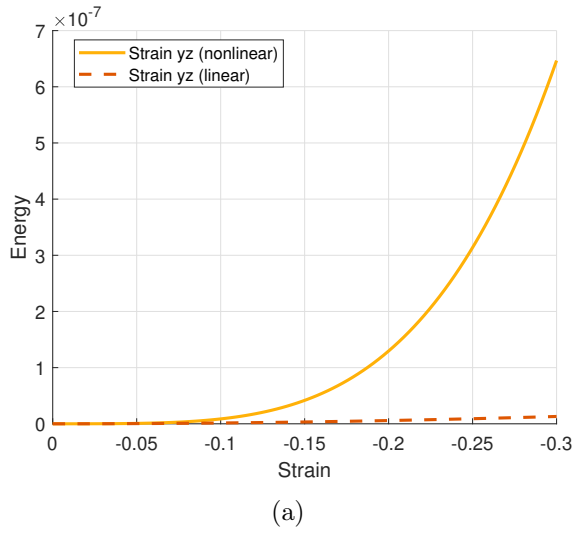


Figure 4.2: Comparison of the strain–energy relation between the linear and geometrically nonlinear models for loading in selected shear directions for (a) unimodal and (b) pentamodal metamaterial.

5 Summary

Our study dealt with optimising metamaterials for desired unimodal and pentamodal behaviour. The material PUCs were modelled as discrete truss systems, whose effective metamaterial properties were determined using the first-order numerical homogenisation, providing us with a link between their microstructure and macroscopic behaviour to be optimised.

We formulated the objective function on the basis of a projected stiffness and sorted eigenvalues of the homogenised stiffness matrix. The unimodal metamaterials were designed to be significantly more compliant in a chosen shear direction compared to other modes of deformation. The pentamodal metamaterial targeted maximal bulk modulus while diminishing the remaining eigenvalues of the homogenised stiffness matrix.

The optimisation process was performed using the steepest ascent method, supplemented with the line search algorithm, and constrained by upper and lower bounds for individual cross-sectional areas. To suppress the algorithm's attraction to local minima, we proposed a simple modification of the steepest ascent, which sequentially performs a series of 1D minimisations along individual design variables. Especially in the case of pentamodal material, this modification significantly improved the optimisation results by reducing the number of independent optimisation runs necessary to render a performant solution.

We subjected the optimised metamaterials to geometrically nonlinear analysis to evaluate their response under large deformations. The structures retained their characteristic multimodal behaviour even under 30% strain in each direction.

Bibliography

- [1] E. Barchiesi, M. Spagnuolo, and L. Placidi, “Mechanical metamaterials: A state of the art,” Mathematics and Mechanics of Solids, vol. 24, no. 1, pp. 212–234, Jan. 2019. DOI: 10.1177/1081286517735695.
- [2] O. Sigmund, “A new class of extremal composites,” Journal of the Mechanics and Physics of Solids, vol. 48, no. 2, pp. 397–428, Feb. 2000. DOI: 10.1016/S0022-5096(99)00034-4.
- [3] G. W. Milton and A. V. Cherkaev, “Which Elasticity Tensors are Realizable?” Journal of Engineering Materials and Technology, vol. 117, no. 4, pp. 483–493, Oct. 1995. DOI: 10.1115/1.2804743.
- [4] A. Martin, M. Kadic, R. Schittny, T. Bückmann, and M. Wegener, “Phonon band structures of three-dimensional pentamode metamaterials,” Physical Review B, vol. 86, no. 15, p. 155 116, Oct. 2012, Publisher: American Physical Society. DOI: 10.1103/PhysRevB.86.155116.
- [5] A. O. Krushynska, P. Galich, F. Bosia, N. M. Pugno, and S. Rudykh, “Hybrid metamaterials combining pentamode lattices and phononic plates,” Applied Physics Letters, vol. 113, no. 20, p. 201 901, Nov. 2018. DOI: 10.1063/1.5052161.
- [6] C. W. Cushing, M. J. Kelsten, X. Su, P. S. Wilson, M. R. Haberman, and A. N. Norris, “Design and characterization of a three-dimensional anisotropic additively manufactured pentamode material,” The Journal of the Acoustical Society of America, vol. 151, no. 1, pp. 168–179, Jan. 2022. DOI: 10.1121/10.0009161.
- [7] C. Gustavo Méndez, J. M. Podestá, O. Lloberas-Valls, S. Toro, A. E. Huepe, and J. Oliver, “Computational material design for acoustic cloaking,” International Journal for Numerical Methods in Engineering, vol. 112, no. 10, pp. 1353–1380, 2017. DOI: 10.1002/nme.5560.
- [8] A. Amendola, G. Carpentieri, L. Feo, and F. Fraternali, “Bending dominated response of layered mechanical metamaterials alternating pentamode lattices and confinement plates,” Composite Structures, vol. 157, pp. 71–77, Dec. 2016. DOI: 10.1016/j.compstruct.2016.07.031.
- [9] P. N. Lympelopoulous and E. E. Theotokoglou, “Computational analysis of pentamode metamaterials for antiseismic design,” Procedia Structural Integrity, 1st Mediterranean Conference on Fracture and Structural Integrity, MedFract1, vol. 26, pp. 263–268, Jan. 2020. DOI: 10.1016/j.prostr.2020.06.033.
- [10] Y. Huang, X. Lu, G. Liang, and Z. Xu, “Pentamodal property and acoustic band gaps of pentamode metamaterials with different cross-section shapes,” Physics Letters A, vol. 380, no. 13, pp. 1334–1338, Mar. 2016. DOI: 10.1016/j.physleta.2016.01.041.
- [11] M. Kadic, T. Bückmann, R. Schittny, P. Gumbsch, and M. Wegener, “Pentamode Metamaterials with Independently Tailored Bulk Modulus and Mass Density,” Physical Review Applied, vol. 2, no. 5, p. 054 007, Nov. 2014. DOI: 10.1103/PhysRevApplied.2.054007.
- [12] B. Kumar, A. Banerjee, and B. Manna, “Effect of finite mass on phononic band structure of face centered pentamodal lattice,” Mechanics Research Communications, vol. 124, p. 103 933, Sep. 2022. DOI: 10.1016/j.mechrescom.2022.103933.

- [13] F. Fraternali and A. Amendola, “Mechanical modeling of innovative metamaterials alternating pentamode lattices and confinement plates,” Journal of the Mechanics and Physics of Solids, vol. 99, pp. 259–271, Feb. 2017. DOI: 10.1016/j.jmps.2016.11.010.
- [14] D. Guo et al., “Ultrahigh compression-shear ratio of sandwich pentamode metamaterials,” Composite Structures, vol. 322, p. 117331, Oct. 2023. DOI: 10.1016/j.compstruct.2023.117331.
- [15] K. Mohammadi, M. R. Movahhedy, I. Shishkovsky, and R. Hedayati, “Hybrid anisotropic pentamode mechanical metamaterial produced by additive manufacturing technique,” Applied Physics Letters, vol. 117, no. 6, p. 061901, Aug. 2020. DOI: 10.1063/5.0014167.
- [16] C. Cai, R. Guo, X. Wang, F. Sun, Z. Wang, and Z. Xu, “Effect of anisotropy on phononic band structure and figure of merit of pentamode metamaterials,” Journal of Applied Physics, vol. 127, no. 12, p. 124903, Mar. 2020. DOI: 10.1063/1.5140610.
- [17] Y. Huang, X. Zhang, M. Kadic, and G. Liang, “Stiffer, Stronger and Centrosymmetrical Class of Pentamodal Mechanical Metamaterials,” Materials, vol. 12, no. 21, p. 3470, Oct. 2019. DOI: 10.3390/ma12213470.
- [18] O. Sigmund, “Materials with prescribed constitutive parameters: An inverse homogenization problem,” International Journal of Solids and Structures, vol. 31, no. 17, pp. 2313–2329, Sep. 1994. DOI: 10.1016/0020-7683(94)90154-6.
- [19] D. Zhang, X. Zhai, L. Liu, and X.-M. Fu, “An optimized, easy-to-use, open-source GPU solver for large-scale inverse homogenization problems,” Structural and Multidisciplinary Optimization, vol. 66, no. 9, p. 207, Sep. 2023. DOI: 10.1007/s00158-023-03657-y.
- [20] P. Vogiatzis, S. Chen, X. Wang, T. Li, and L. Wang, “Topology optimization of multi-material negative Poisson’s ratio metamaterials using a reconciled level set method,” Computer-Aided Design, vol. 83, pp. 15–32, Feb. 2017. DOI: 10.1016/j.cad.2016.09.009.
- [21] S. Watts and D. A. Tortorelli, “A geometric projection method for designing three-dimensional open lattices with inverse homogenization,” International Journal for Numerical Methods in Engineering, vol. 112, no. 11, pp. 1564–1588, Dec. 2017. DOI: 10.1002/nme.5569.
- [22] F. Wang, O. Sigmund, and J. Jensen, “Design of materials with prescribed nonlinear properties,” Journal of the Mechanics and Physics of Solids, vol. 69, pp. 156–174, Sep. 2014. DOI: 10.1016/j.jmps.2014.05.003.
- [23] H.-W. Dong et al., “Customized broadband pentamode metamaterials by topology optimization,” Journal of the Mechanics and Physics of Solids, vol. 152, p. 104407, Jul. 2021. DOI: 10.1016/j.jmps.2021.104407.
- [24] Z. Li, Z. Luo, L.-C. Zhang, and C.-H. Wang, “Topological design of pentamode lattice metamaterials using a ground structure method,” Materials & Design, vol. 202, p. 109523, Apr. 2021. DOI: 10.1016/j.matdes.2021.109523.
- [25] Z. Zou, F. Xu, Y. Pan, and T. Fang, “Bandgap properties and multi-objective optimization of double-cone pentamode metamaterials with curved side,” Physica Scripta, vol. 98, no. 3, p. 035833, Mar. 2023. DOI: 10.1088/1402-4896/acb5cc.

- [26] J. Michel, H. Moulinec, and P. Suquet, “Effective properties of composite materials with periodic microstructure: A computational approach,” Computer Methods in Applied Mechanics and Engineering, vol. 172, no. 1-4, pp. 109–143, Apr. 1999. DOI: 10.1016/S0045-7825(98)00227-8.
- [27] M. Doškář and J. Novák, “A jigsaw puzzle framework for homogenization of high porosity foams,” Computers & Structures, vol. 166, pp. 33–41, Apr. 2016. DOI: 10.1016/j.compstruc.2016.01.003.
- [28] N. Jošková and M. Doškář, “Effect of geometry on homogenised properties of selected auxetic metamaterials,” Acta Polytechnica CTU Proceedings, vol. 49, pp. 20–25, Nov. 2024. DOI: 10.14311/APP.2024.49.0020.
- [29] J. Nocedal and S. J. Wright, Numerical optimization (Springer series in operations research), 2nd ed. New York: Springer, 2006, ISBN: 978-0-387-30303-1.
- [30] K. Svanberg, “The method of moving asymptotes—a new method for structural optimization,” International Journal for Numerical Methods in Engineering, vol. 24, no. 2, pp. 359–373, Feb. 1987. DOI: 10.1002/nme.1620240207.
- [31] T. Belytschko, Nonlinear Finite Elements for Continua and Structures (New York Academy of Sciences Series), 1st ed. Newark: John Wiley & Sons, Incorporated, 2014, ISBN: 978-1-118-63270-3 978-1-118-70005-1.